Mechanistically Guided Materials Chemistry: Synthesis of Ternary Nitrides, CaZrN$_2$ and CaHfN$_2$

Christopher L. Rom, Andrew Novick, Matthew J. McDermott, Andrey A. Yakovenko, Jessica R. Gallawa, Gia Thinh Tran, Dominic C. Asebiah, Emily N. Storck, Brennan C. McBride, Rebecca C. Miller, Amy L. Prieto, Kristin A. Persson, Eric Toberer, Vladan Stevanović, Andriy Zakutayev, and James R. Neilson*

Read Online

ACCESS | Metrics & More | Article Recommendations | Supporting Information

ABSTRACT: Recent computational studies have predicted many new ternary nitrides, revealing synthetic opportunities in this underexplored phase space. However, synthesizing new ternary nitrides is difficult, in part because intermediate and product phases often have high cohesive energies that inhibit diffusion. Here, we report the synthesis of two new phases, calcium zirconium nitride (CaZrN$_2$) and calcium hafnium nitride (CaHfN$_2$), by solid state metathesis reactions between Ca$_3$N$_2$ and MCl$_4$ (M = Zr, Hf). Although the reaction nominally proceeds to the target phases in a 1:1 ratio of the precursors via Ca$_3$N$_2$ + MCl$_4$ → CaMN_2 + 2 CaCl$_2$, reactions prepared this way result in Ca-poor materials (Ca$_x$$M_{2-x}N_2$, $x < 1$). A small excess of Ca$_3$N$_2$ (ca. 20 mol %) is needed to yield stoichiometric CaMN_2, as confirmed by high-resolution synchrotron powder X-ray diffraction. *In situ* synchrotron X-ray diffraction studies reveal that nominally stoichiometric reactions produce Zr^{3+} intermediates early in the reaction pathway, and the excess Ca$_3$N$_2$ is needed to reoxidize Zr^{3+} intermediates back to the Zr^{4+} oxidation state of CaZrN$_2$. Analysis of computationally derived chemical potential diagrams rationalizes this synthetic approach and its contrast from the synthesis of MgZrN$_2$. These findings additionally highlight the utility of *in situ* diffraction studies and computational thermochemistry to provide mechanistic guidance for synthesis.

INTRODUCTION

Predictive synthesis remains an important goal for materials chemists.[1−3] While many joint computational-experimental synthesis efforts have been reported in literature,[4−17] trial-and-error approaches remain the dominant paradigm. Within this current paradigm, *in situ* X-ray diffraction (XRD) is a powerful technique for materials discovery.[16,18−22] Sometimes called "panoramic synthesis,"[18−20,22] *in situ* X-ray diffraction allows for observation of solid-state reactivity as it happens. Short-lived intermediate species and subtle crystallographic changes can be detected that would otherwise be missed by *ex situ* experiments, accelerating materials discovery. In a move toward predictive synthesis, *in situ* XRD has been used in concert with computationally generated chemical potential diagrams[23] to rationalize polymorph selectivity in the synthesis of ternary oxides.[24] However, this specific combined approach of *in situ* XRD and chemical potential diagrams has yet to be used to discover new materials.

Nitrides are a compelling class of materials for melding computational guidance with *in situ* XRD studies, because they are difficult to synthesize. High-temperatures are often needed to overcome the relative inertness of N$_2$ (945 kJ/mol dissociation energy)[25] and drive solid state diffusion.[26,27] The strength of the N$_2$ triple bond also results in smaller formation energies for nitrides compared to oxides.[28] These small formation energies, combined with the entropic favorability

of forming a gas (i.e., N$_2$) at elevated temperatures via decomposition of a nitride to metal and N$_2$(g), leads many nitrides to decompose at elevated reaction temperatures.[29,30] Therefore, successful syntheses may be limited to narrow temperature windows, which *in situ* XRD can help identify.[31]

Discovering synthetic routes to nitrides can unlock world changing technologies. For example, the development of controlled crystal growth and substitution strategies for (In,Ga)N enabled high-efficiency light emitting diodes and earned the Nobel Prize in Physics in 2014.[32] Advancing synthesis science will make more discoveries like this possible. Recent computational studies have predicted numerous stable phases in previously uncharted spaces,[4,11,33−35] accelerating the discovery of new ternary nitrides (e.g., MgSnN$_2$,[36,37] CaSnN$_2$,[38] and MgZrN$_2$[39,40]). Yet many predicted phases remain undiscovered, providing copious targets for synthesis.

All of the ABN$_2$ phases (A = Mg, Ca, Sr, Ba; B = Ti, Zr, Hf) have been synthesized previously,[39,41−44] with the exception of

Figure 1. ABN_2 ternaries with larger alkali earth cations (Sr and Ba) crystallize in cation-ordered phases of the KCoO$_2$-type (brown X's) and α-NaFeO$_2$-type structures (green triangles), while MgBN$_2$ phases take the rocksalt (RS) structure (blue squares). This work shows that CaZrN$_2$ and CaHfN$_2$ crystallize in the cation-disordered RS structure (outlined squares). Adapted with permission from ref 45. Copyright 1969, International Union of Crystallography.

CaZrN$_2$ and CaHfN$_2$.[29] As summarized in Figure 1, these phases crystallize with several structure types: rocksalt ($Fm\overline{3}m$), KCoO$_2$-type ($P4/nmm$), and α-NaFeO$_2$-type ($R\overline{3}m$). Given the intermediate size of Ca^{2+} relative to the other alkali earths (Figure 1),[45] CaZrN$_2$ and CaHfN$_2$ were predicted to crystallize in the α-NaFeO$_2$ structure type.[46] However, syntheses of CaZrN$_2$ and CaHfN$_2$ have not been previously reported, although one group described some synthetic attempts toward these ternaries that yielded only ZrN and HfN.[47]

Here, we report the discovery of CaZrN$_2$ and CaHfN$_2$ in the disordered rocksalt (RS) structure via a metathesis approach. Heating Ca$_3$N$_2$ and ZrCl$_4$ or HfCl$_4$ to a high-temperature dwell (ca. 1000 °C) for a brief period of time (10 min) yields CaZrN$_2$ and CaHfN$_2$ as fine powders (along with a byproduct CaCl$_2$). Importantly, a slight excess of Ca$_3$N$_2$ is needed, a fact we rationalize based on our *in situ* synchrotron X-ray diffraction studies and computational thermodynamic analysis of the reaction pathway that show reduced Zr^{3+} intermediates. Chemical potential diagrams rationalize the thermodynamics behind the observed reactions, accurately predicting differences in the reaction pathway between the reactions targeting CaZrN$_2$ vs MgZrN$_2$ vs ZnZrN$_2$ (which has not yet been synthesized in bulk). Additional thermodynamic calculations show that these disordered RS ternaries are metastable (relative to the cation-ordered polymorph), even at high synthesis temperatures. In sum, these findings show how chemical potential diagrams can augment *in situ* XRD experiments and improve our ability to predict synthesis pathways.

■ RESULTS AND DISCUSSION

Structural and Compositional Analysis. High-resolution synchrotron powder X-ray diffraction (SXRD) measurements show that metathesis reactions between Ca$_3$N$_2$ and MCl$_4$ (M = Zr, Hf) yielded CaZrN$_2$ and CaHfN$_2$ in the RS structure ($Fm\overline{3}m$, Figure 2). These samples (1.21 Ca$_3$N$_2$ + ZrCl$_4$ and 1.16 Ca$_3$N$_2$ + HfCl$_4$) were heated at +5 °C/min to 1100 °C, dwelled for 10 min, and then air-quenched to yield CaMN$_2$ along with an array of side products (CaCl$_2$, Ca$_2$NCl, Ca$_4$Cl$_6$O, and in the case of M = Hf, trace HfN). Recovered samples were black, red, or green, depending on the precise synthesis conditions (Figure S1). Washing the samples with anhydrous methanol removes the chloride-containing byproducts (CaCl$_2$, Ca$_2$NCl, Ca$_4$Cl$_6$O). However, one unindexed diffraction peak is present at Q = 0.8 Å^{-1}. This peak matches both the (100) reflection from Ca$_4$Cl$_6$O and the most intense reflection in a prior report of calcium methoxide.[48] Qualitative inspection of our patterns suggests calcium methoxide is more likely, as this Q = 0.8 Å^{-1} peak is the only strong reflection in the literature report for that compound,[48] and the other reflections for Ca$_4$Cl$_6$O are absent. Unfortunately, the presence

Figure 2. SXRD data of (a) CaZrN$_2$ as synthesized and (b) washed along with (c) CaHfN$_2$ as synthesized and (d) washed. Simulated patterns for relevant phases are shown for reference (top). The predicted, ordered structure ($R\overline{3}m$) of CaMN$_2$ was not observed. A single impurity peak appears after washing (marked by an asterisk and fit with a single pseudovoigt peak), possibly a disordered Ca$_4$Cl$_6$O or calcium methoxide. Dashed gray vertical lines guide the eye to the (111), (200), and (220) reflections of CaMN$_2$ $Fm\overline{3}m$. Full diffraction patterns are shown in Figure S2, and refinement results are given in Tables S1−S2 and Figure S3.

of the impurity phase inhibits accurate compositional analysis by Scanning Electron Microscopy (SEM) with Energy Dispersive X-ray Spectroscopy (EDS), rigorously air-free X-ray Photoelectron Spectroscopy (XPS), and combustion analysis (further described in the Supporting Information, Figures S5−S8 and Tables S3−S4).[49−52] Consequently, our characterization efforts were centered on diffraction.

Rietveld analysis of the RS products shows these phases are consistent with cation-disordered $CaZrN_2$ and $CaHfN_2$. The metal site occupancy (x in $Ca_x M_{2-x}N_2$) was refined to 1.00(2) for the washed $CaZrN_2$ and 1.00(1) for the washed $CaHfN_2$ sample. Washing does not substantially change the refined metal site occupancy or lattice parameter compared with the samples as synthesized (Figure S3). Lattice parameters of the washed $CaMN_2$ phases refined to substantially larger unit values (a = 4.7486(3) Å and 4.7224(4) Å for $CaZrN_2$ and $CaHfN_2$, respectively) than their isostructural binaries (a = 4.585(2) Å and 4.5210(2) Å for ZrN and HfN, respectively).[53,54] These ternary unit cell values are close to the Ca−N−Zr distance in the computationally predicted, cation-ordered $CaZrN_2$ structure (4.744 Å), which serves as an estimate for the theoretical disordered RS lattice parameter (Figure S4). We focused most of our work on the Zr analogue, since Zr and Hf exhibit analogous chemistry in this case.

A slight excess of Ca_3N_2 (ca. 20 mol %) is required to yield stoichiometric $CaZrN_2$ (Figure 3), as measured by the product

Figure 3. (a) The precursor ratio (expressed as n in nCa_3N_2 + $ZrCl_4$) impacted the lattice parameter of the RS phase and (b) the distribution of byproduct phases, as determined by Rietveld analysis. Approximately 20% mole excess (n = 1.2) Ca_3N_2 was necessary to yield stoichiometric $CaZrN_2$, as indicated by the estimated value of a = 4.744 Å from the computationally predicted structure (Figure S4). However, some excess Ca_3N_2 also yielded a Ca_2NCl byproduct by reacting with $CaCl_2$ (b). The byproduct relative mol % of $CaCl_2$, Ca_2NCl, and Ca_4Cl_6O sum to 100% (i.e., $Ca_xZr_{2-x}N_2$ is not included owing to uncertainty in x). These data were from samples held in alumina crucibles sealed in ampules under vacuum, heated at 5 °C/min to 1000 °C, dwelled for 10 min, then quenched by removing the ampule from the furnace and placing it on the benchtop.

lattice parameter. Although the nominal balanced equation for the reaction is Ca_3N_2 + $ZrCl_4$ → $CaZrN_2$ + 2 $CaCl_2$, a 1:1 precursor ratio yields a lattice parameter of 4.718(1) Å, trending toward ZrN and suggesting a Ca-poor phase. With an additional 20 mol % Ca_3N_2 (i.e., n = 1.20), the RS lattice parameter is closer to the 4.744 Å value estimated from the computationally predicted structure (Figure S4). The continued growth in the RS lattice parameter above n = 1.20 could suggest the formation of Ca interstitials, but character-

izing such defects is beyond the scope of this study. This trend contrasts with our prior synthesis of $MgZrN_2$, where the stoichiometric reaction 2.0 Mg_2NCl + $ZrCl_4$ → $MgZrN_2$ + 3 $MgCl_2$ produced the targeted ternary (RS $MgZrN_2$), and additional Mg_2NCl did not change the RS lattice parameter or increase Mg content (as measured by SXRD, Inductively Coupled Plasma Atomic Emission Spectroscopy, and Energy Dispersive X-ray Spectroscopy).[40] Some of the excess Ca_3N_2 reacts with the $CaCl_2$ byproduct to make Ca_2NCl, which is observed in an increasing mol % with increasing Ca_3N_2 content. The need for excess Ca_3N_2 is not attributable to the oxide impurity in the Ca_3N_2 precursor, which is estimated at <5 wt % of our precursor by quantitative Rietveld analysis (below the detection limit of laboratory PXRD). We also note that increasing the dwell time from 10 min to 4 h did not substantially change the RS lattice parameter, size, or strain for Ca-rich reactions (2.0 Ca_3N_2 + $ZrCl_4$, T_{rxn} = 1000 °C, Figure S10). Increasing the temperature decreases the lattice parameter but increases the crystallite size (1.2 Ca_3N_2 + $ZrCl_4$, dwell time = 10 min, Figure S11). Furthermore, increasing dwell times for Ca-poor reactions decreases the rocksalt lattice parameter (dwell temperature = 900 °C; Figure S12). The key observation is that some excess Ca_3N_2 is necessary. This result is explained by observations from our *in situ* SXRD measurements, as discussed in the next section.

Using metathesis (ion exchange) reactions is also a key synthetic choice for the synthesis of $CaZrN_2$, as this process circumvents the solid-state diffusion challenges common to traditional ceramic syntheses.[55,56] A control reaction between Ca_3N_2 and Zr under flowing N_2 at 1000 °C for 10 h produces only ZrN alongside unreacted Ca_3N_2, indicating that Ca diffusion into ZrN is slow (Figure S13). Literature also shows the difficulty of making $CaZrN_2$ and $CaHfN_2$. In their report on the synthesis of Ca_4TiN_4 and Ca_5NbN_5 with the assistance of a Li_3N flux, Hunting et al. noted that similar reactions between Ca_3N_2 and Zr or Hf powders in Li_3N flux only yielded the ZrN and HfN.[47] And although many closely related compounds have been synthesized by ceramic techniques (i.e., $CaTiN_2$, $SrZrN_2$, $BaZrN_2$),[41,43,57] the absence of $CaZrN_2$ and $CaHfN_2$ from the literature implies that a synthetic strategy had previously been elusive.

***In Situ* Synchrotron Powder X-ray Diffraction.** *In situ* synchrotron powder X-ray diffraction studies (SXRD) at the Advanced Photon Source (17-BM) reveal the pathway through which the metathesis reactions proceed. We examined reactions in sealed quartz capillaries targeting $CaZrN_2$ (and $MgZrN_2$, for comparison) starting from reagent mixtures for ideal reactions: A_3N_2 + $ZrCl_4$ →$AZrN_2$ + 2 ACl_2 and 2 A_2NCl + $ZrCl_4$ → $AZrN_2$ + 3 ACl_2 (A = Mg, Ca). These ratios are calcium-deficient compared to the optimized synthesis of $CaZrN_2$ discussed previously yet are nonetheless illuminating. They show how ostensibly similar precursors (A_3N_2 and A_2NCl) proceed via different reaction pathways. These differences in the reaction pathway ultimately required different synthetic conditions for the optimized syntheses of $MgZrN_2$ and $CaZrN_2$. The relative amounts of crystalline phases present during the reaction (determined by quantitative phase analysis using the Rietveld method of *in situ* diffraction data) are shown in Figure 4, with the raw diffraction patterns shown in Figures S17 and S18. The observed Zr-containing intermediates are summarized in Table 1.

Quantitative phase analysis of *in situ* SXRD data from the reaction between Ca_3N_2 + $ZrCl_4$ show that reduced Zr^{3+}

Figure 4. Phase contributions to the *in situ* SXRD data as a function of temperature as indicated by the weighted scale factors (W.S.F.) for reactants, intermediates, and products upon heating precursor mixtures of (a) Ca_3N_2 + $ZrCl_4$, (b) Mg_3N_2 + $ZrCl_4$, (c) 2 Ca_2NCl + $ZrCl_4$, and (d) 2 Mg_2NCl + $ZrCl_4$. In reactions with Mg_3N_2, Ca_3N_2, and Ca_2NCl, trivalent Zr species were observed ($ZrCl_3$ and Zr_6NCl_{15}), indicating a reduction of Zr^{4+} to Zr^{3+} and loss of N_2. Only the reaction using Mg_2NCl maintained the tetravalent oxidation state of Zr. The ternary phases $Ca_xZr_{2-x}N_2$ and $Mg_xZr_{2-x}N_2$ are denoted as "RS". The gray highlighted region of (d) shows the temperature range used for step 1 of the two-step synthesis of $MgZrN_2$ detailed in prior reports.[40,58]

Table 1. Summary of Zr-Containing Intermediates Observed via the *in Situ* SXRD Studies Shown in Figure 4

Reaction	Zr-containing intermediates			
Ca_3N_2 + $ZrCl_4$	$ZrCl_3$	Zr_6NCl_{15}		
2 Ca_2NCl + $ZrCl_4$	$ZrCl_3$	Zr_6NCl_{15}	$ZrNCl$	
Mg_3N_2 + $ZrCl_4$		Zr_6NCl_{15}	$ZrNCl$	$MgZrCl_6$
2 Mg_2NCl + $ZrCl_4$			$ZrNCl$	$MgZrCl_6$

species form at low reaction temperatures (Figure 4a). $ZrCl_3$ is the first intermediate to form, appearing by 200 °C. Subsequently, $ZrCl_4$ disappears from the patterns as it sublimes (T_{sub} = 331 °C), at which point $CaCl_2$ begins to grow in. Near 400 °C, $ZrCl_3$ converts to a nitride chloride, Zr_6NCl_{15}. Throughout this process, the Ca_3N_2 precursor steadily declines. Ca_3N_2 is fully consumed by 600 °C, with some of it reacting with the $CaCl_2$ byproduct to make Ca_2NCl (Ca_3N_2 + $CaCl_2$ → 2 Ca_2NCl). Ca_2NCl persists up to 700 °C. By ca. 550 °C, the RS phase $Ca_xZr_{2-x}N_2$ begins to grow in (initially as ZrN, as detailed subsequently). A minor phase of Ca_4Cl_6O also grows, indicating a small degree of oxygen impurity. The reaction of 2 Ca_2NCl + $ZrCl_4$ proceeds in a similar fashion as that of Ca_3N_2 + $ZrCl_4$. However, using Ca_2NCl also includes a ZrNCl-like intermediate, which is not detected in the Ca_3N_2 reaction (Figure S17). In summary, the initial reaction between Ca_3N_2 + $ZrCl_4$ proceeds through Zr^{3+} intermediates via the following balanced equations:

$$Ca_3N_2 + 6ZrCl_4 \rightarrow 6ZrCl_3 + N_2 + 3CaCl_2 \quad (1)$$

$$Ca_3N_2 + 12ZrCl_3 \rightarrow 2Zr_6NCl_{15} + 3CaCl_2 \quad (2)$$

$$5Ca_3N_2 + 2Zr_6NCl_{15} \rightarrow 12ZrN + 15CaCl_2 \quad (3)$$

The final step of this process involves the reaction of the Ca_2NCl intermediate with the ZrN rocksalt phase:

$$4Ca_2NCl + 6ZrN + N_2 \rightarrow 6CaZrN_2 + 2CaCl_2 \quad (4)$$

In contrast, the analysis of *in situ* SXRD data in the analogous Mg system shows reactivity differences between Mg_3N_2 and Mg_2NCl, with Mg_2NCl conserving the tetravalent oxidation

state of Zr^{4+} throughout the reaction pathway (Figure 4b and d, Table 1). The observed reaction pathways are consistent with our prior (lower resolution) *in situ* study on the synthesis of $MgZrN_2$.[40] Both the reaction of Mg_3N_2 + $ZrCl_4$ and the reaction of 2Mg_2NCl + $ZrCl_4$ begin with $ZrCl_4$ sublimation, followed by the formation of a small amount of ZrNCl and $MgZrCl_6$ near 300 °C. $MgZrCl_6$ probably forms via reaction between $ZrCl_4$ and the byproduct $MgCl_2$ that is produced alongside the ZrNCl. This small amount of crystalline $MgZrCl_6$ is likely in equilibrium with a substantial amount of $ZrCl_4$ (g).[59] The reaction with Mg_3N_2 goes on to produce Zr_6NCl_{15} near 430 °C, which indicates the reduction of Zr^{4+} to Zr^{3+}, likely paired with the production of N_2. Furthermore, the amount of Mg_3N_2 only decreases slightly by 600 °C (at which point the measurement was stopped). This result suggests that Mg_3N_2 is a kinetically slow precursor. On the other hand, the Mg_2NCl reaction does not produce any distinct Zr^{3+} intermediates. Instead, the amount of Mg_2NCl decreases in a stepwise fashion near 440 °C coincident with the rapid increase of ZrNCl and $MgCl_2$. A second stepwise decrease in Mg_2NCl occurs near 600 °C, coincident with the consumption of ZrNCl and the formation of the RS phase ($Mg_xZr_{2-x}N_2$). Therefore, the synthesis of $MgZrN_2$ appears to proceed through two reaction steps:

$$Mg_2NCl + ZrCl_4 \rightarrow ZrNCl + 2MgCl_2 \quad (5)$$

$$Mg_2NCl + ZrNCl \rightarrow MgZrN_2 + MgCl_2 \quad (6)$$

The $MgZrCl_6$ intermediate likely behaves similarly to its equilibrium components (i.e., $MgZrCl_6 \rightleftharpoons MgCl_2 + ZrCl_4$). As noted in prior reports, heating directly to a high temperature (ca. 800 °C) results in an Mg-poor RS phase, but a two-step process yields stoichiometric $MgZrN_2$.[40,58] The first step of that two-step process (T_{react}) is a 12 to 24 h dwell at 450−500 °C (the highlighted gray temperature region in Figure 4), likely where eqs 5 and 6 proceed to completion. The second heating step (to T_{cryst} = 800 °C) aids in the crystallization of amorphous/nanocrystalline $MgZrN_2$. This *in situ* study reveals how the two-step process allows the synthesis of $MgZrN_2$ to

proceed through a single Zr^{4+} intermediate, whereas the synthesis of $CaZrN_2$ must proceed through Zr^{3+} intermediates that require subsequent reoxidation (Table 1).

The lattice parameter, a, of the disordered rocksalt $Ca_xZr_{2x}N_2$ formed during the $Ca_3N_2 + ZrCl_4$ reaction shows that the ZrN intermediate from eq 3 reacts with Ca_2NCl to form $CaZrN_2$ (Figure 5). As the RS phase grows in between

Figure 5. (a) Weighted scale factor (W.S.F.) as a function of temperature for the $Ca_3N_2 + ZrCl_4$ reaction and (b) refined lattice parameter a for the RS $Ca_xZr_{2-x}N_2$ obtained from Rietveld analysis of the in situ SXRD data. The opacity of the RS markers in (b) is normalized to the W.S.F. in (a). The lattice parameters for $CaZrN_2$ at room temperature is shown for reference, along with the value of ZrN accounting for thermal expansion (adapted with permission from ref 60 (Copyright 1964, Elsevier). The increase in a for $Ca_xZr_{2-x}N_2$ suggests Ca uptake from the Ca_2NCl intermediate. When the Ca_2NCl intermediate is fully consumed (vertical dashed line), the RS lattice parameter begins to contract, suggesting Ca loss.

500 and 600 °C, the lattice parameter closely matches the value expected for ZrN by thermal expansion.[60] Between 520 and 570 °C, the apparent decrease in the parameter is an artifact of the broad, low-intensity peaks that are difficult to accurately fit. Above 570 °C, the parameter expands up to 4.674 Å by 725 °C. The expansion concomitant with the decreasing W.S.F. of Ca_2NCl suggests calcium uptake by ZrN from the Ca_2NCl intermediate across a solid solution $Ca_x Zr_{2-x} N_2$ ($0 \leq x \leq 1$), with Zr^{3+} to Zr^{4+} oxidation driven by N_2 reincorporation:

$$4xCa_2NCl + (12 - 6x)ZrN + xN_2$$
$$\rightarrow 6Ca_xZr_{2-x}N_2 + 2xCaCl_2 \qquad (7)$$
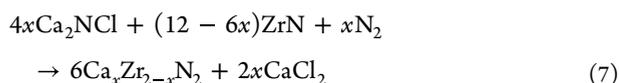
Above 725 °C, the RS lattice parameter decreases. This inflection point occurs at the same temperature at which Ca_2NCl is fully consumed. The contraction of the lattice parameter is consistent with a loss of calcium from the structure, possibly by reaction with oxygen from the quartz container ($2 Ca_xZr_{2-x}N_2 + x SiO_2 \rightarrow 2x CaO + (4-2x) ZrN + x N_2 + x Si$).

This pathway shows why "excess" Ca_3N_2 is required for $CaZrN_2$ formation: it provides the necessary oxidant, N_2. The N_2 likely comes from the reincorporation of the released nitrogen yielded during Zr^{3+} formation (eq 1), although alternative hypotheses are considered in the Supporting Information (eqs S1 and S2). While this process may seem similar to the ceramic reaction discussed previously (Figure

S13), the ZrN crystallites formed in situ via metathesis are very small (ca. 10 nm) compared to the ZrN formed via the ceramic route (ca. 1 μm) and may contain a significant fraction of point defects, facilitating diffusion. These differences allow the metathesis-produced ZrN to react to form $CaZrN_2$ within a 10 min dwell, while the ceramic route is impractically slow. To test the eq 7 hypothesis, we reacted 2 $Ca_3N_2 + ZrCl_4$ at 1000 °C under flowing N_2 for 4 h (Figure S13). The resulting PXRD data of the red powder were well described by rocksalt $CaZrN_2$ (a = 4.7658(4) Å) with Ca_2NCl as the only byproduct. Furthermore, thermodynamic calculations (see the next section) suggest eq 7 is a thermodynamically favorable step.

Thermodynamic Analysis of the Reaction Pathway. The chemical potential diagrams shown in Figure 6 describe the energetic landscape through which these metathesis reactions proceed. These models are computed using calculated phase energies from the Materials Project database[61] (see Experimental Section). Each visible facet is a stable phase in the $A-Zr-Cl$ system; larger facets indicate phases with deeper stability on the convex hull of a compositional phase diagram relative to competing phases. Nitrogen-containing phases are illustrated by 3-dimensional ($A-Zr-Cl$) polyhedral slices of the full 4-dimensional polytopes. Intersection points, edges, or faces between these regions of the chemical potential space indicate which phases share stable interfaces. It has previously been observed that a chemical reaction proceeding under local equilibrium (i.e., diffusion-controlled) conditions will follow a pathway between adjacent phases.[2,24]

Figure 6a and c show that no Zr^{4+}-containing species in the $Ca-Zr-N-Cl$ phase space shares a stable interface with the $CaZrN_2$ product, indicating that Zr^{3+}-containing intermediates must form if the system proceeds through local equilibrium at interfaces. Specifically, the region of stability for ZrN connects both the Zr_6NCl_{15} and ZrNCl spaces to the $CaZrN_2$ space, indicating that ZrN should form along the pathway to $CaZrN_2$. In reality, due to the accommodation of off-stoichiometry, there is likely no sharp boundary (discontinuity) between ZrN and $CaZrN_2$.[23] Rather, this sharp transition is due to the limitations of our thermodynamic data, as only ordered stoichiometric compounds are permitted in the DFT calculations of the Materials Project database. We discuss the stability of cation-disordered $CaZrN_2$ further in the next section and in the Supporting Information (Figure S21).

The chemical potential diagram for the $Mg-Zr-N-Cl$ system (Figure 6b) appears similar to that for the Ca system but with one key difference: ZrNCl shares a stable interface with precursor $ZrCl_4$, intermediate $MgZrCl_6$, and product $MgZrN_2$ (Figure 6d). This shared boundary suggests that the intermediate ZrNCl (a Zr^{4+}-containing phase) facilitates the formation of $MgZrN_2$ at the $ZrCl_4|Mg_2NCl$ interface while preventing the system from undergoing Zr- and N-based reduction and oxidation. The $MgZrCl_6$ intermediate behaves similarly. It is the closest Mg-containing phase to form from $ZrCl_4$, some of which likely reacts with the $MgCl_2$ produced as a byproduct of ZrNCl formation. $MgZrCl_6$ then decomposes into $MgCl_2$ and ZrNCl.

Reaction network analysis[62] can quantify these differences between the Ca- and $Mg-Zr-N-Cl$ systems. The method calculates a distance in the chemical potential space, simplifying these geometric representations into numeric values. The chemical potential distance for the reaction of $Ca_2NCl + ZrNCl \rightarrow CaZrN_2 + CaCl_2$ is 0.733 eV/atom, where the nonzero number means that the reactants and products do
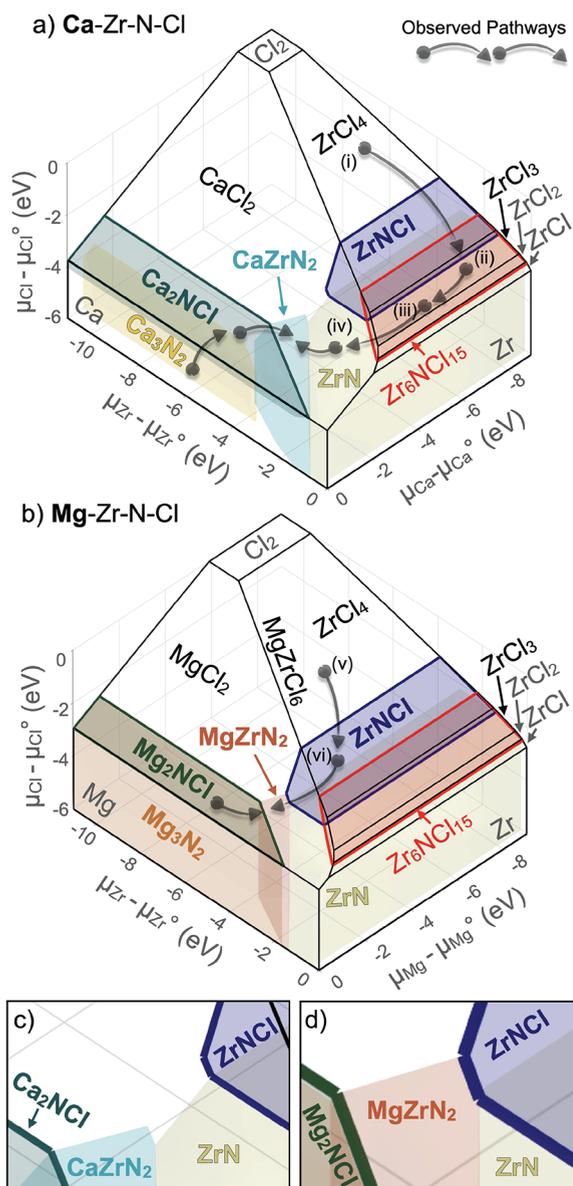
Figure 6. Chemical potential diagrams for (a) the Ca−Zr−N-Cl chemical system and (b) the Mg−Zr−N−Cl chemical system calculated for 300 °C. Focused view highlighting the interfaces between ZrNCl and (c) Ca_2NCl or (d) Mg_2NCl. Select nitrogen-containing phases in the 4-component system are illustrated via their intersection with the 3-dimensional $\mu_{Ca} - \mu_{Zr} - \mu_{Cl}$ or $\mu_{Mg} - \mu_{Zr} - \mu_{Cl}$ spaces. These intersections may appear with complicated volumes due to the lower dimensional intersection (e.g., $CaZrN_2$, ZrN). Full quaternary diagrams are shown in Figure S22. Curved arrows qualitatively illustrate the experimentally observed reaction pathways.

not share stable interfaces (as visualized in Figure 6c). In contrast, $Mg_2NCl + ZrNCl \rightarrow MgZrN_2 + MgCl_2$ (Figure 6d) has a chemical potential distance of 0.033 eV/atom, which is only nonzero because of how metastable phases like Mg_2NCl are calculated. Further details are in the Supporting Information (Tables S5−S13).

The chemical potential diagram boundaries are consistent with those from the *in situ* SXRD measurements. For the Ca-system, the annotated reaction arrows in Figure 6a correspond to the intermediates observed to form by *in situ* SXRD (Figure 4), and the progression from ZrN to $CaZrN_2$ via a $Ca_xZr_{2-x}N_2$

solid solution (Figure 5): arrow (i) represents eq 1, arrow (ii) eq 2, arrow (iii) eq 3, and arrow (iv) eq 4 (or an alternative hypothesis, eqs S1, S2). Similarly, the chemical potential diagram for the Mg-system also matches the observed behavior of the $Mg_2NCl + ZrCl_4$ reaction: arrow (v) represents eq 5 and arrow (vi) represents eq 6. While analysis of these diagrams prior to experiment may not predict the exact reaction pathway,[23] these diagrams show the thermodynamic possibilities and limitations.

This mechanistic guidance provided the key insight that ultimately led to our successful syntheses. As the Ca−Zr−N−Cl chemical potential diagram (Figure 6a, c) shows that ZrN formation is unavoidable along the path to $CaZrN_2$, we changed our synthesis conditions (relative to the two-step synthesis of $MgZrN_2$)[40] to deal with the refractory ZrN intermediate. Specifically, we used Ca_3N_2 in a slight excess to provide an oxidant, and we increased our reaction temperature to increase diffusion. We also used only one heating step, as a low temperature step would not avoid Zr^{4+} reduction (whereas in the case of $MgZrN_2$, the two-step process maintained the oxidation state of Zr^{4+}).[40] These changes led to the successful syntheses shown in Figure 2.

Importantly, these chemical potential diagrams can also be used to identify thermodynamically disfavored reactions, allowing researchers to quickly move beyond systems that are unlikely to work. To demonstrate this point, we also conducted metathesis syntheses and thermodynamic calculations targeting $ZnZrN_2$ from 1.2 $Zn_3N_2 + ZrCl_4$ and 2.4 $Zn_2NCl + ZrCl_4$ (Figures S19 and S20). $ZnZrN_2$ has been synthesized via combinatorial sputtering of thin films[15] but has not yet been synthesized in bulk. Our *in situ* SXRD experiments and thermodynamic analysis reveal that the phase is unlikely to be synthesized via metathesis without significantly increasing μ_N. The chemical potential diagrams calculated as a function of temperature show that while $ZnZrN_2$ is predicted to be stable at room temperature, it becomes destabilized at the more synthetically relevant temperature of 300 °C (Figure S19). Instead, ZrNCl and ZrN are calculated to be the main thermodynamic products. *In situ* SXRD measurements confirm these predictions (Figure S20). Although these calculations do not rule out the possibility of $ZnZrN_2$ forming as a kinetic product, they do show that reactions proceeding through local thermodynamic equilibrium at elevated temperature and ambient N_2 pressure will not yield the targeted phase. These chemical potential diagrams therefore serve as powerful tools to accelerate materials discovery via mechanistically guided synthesis.

Several shortcomings limit the predictive ability of chemical potential diagrams. First, chemical potential diagrams with >3 dimensions may obscure certain phases: the 4-dimensional chemical potential diagrams shown here are only visualized in 3-dimensions of chemical potential (μ_A, μ_{Zr}, and μ_{Cl}) with *select* N-containing phases shown as intersections with the 3-dimensional space. Fortunately, quaternary compositional phase diagrams provide complementary and complete, but complicated, visualization (Figure S22). The reaction steps observed *in situ* follow alkemade lines in the quaternary phase diagrams (e.g., reactions that share boundaries on the chemical potential diagram). The geometric distances for *n*-dimensional chemical spaces can also be calculated numerically using reaction network analysis[62] as further discussed in the Supporting Information (Tables S5−S14). Chemical potential diagrams also lack true kinetic information; they can only

illustrate effective kinetic barriers provided by the need for a reaction to form an additional intermediate phase to establish local equilibrium.[2] Lastly, they are limited by the phases in the computational databases (e.g., Materials Project). These databases, while large and growing larger, are incomplete.[4] They also contain only ordered phases (not the disordered structures we observe).

Metastability of Cation Disorder in CaZrN$_2$. The observed disorder in CaZrN$_2$ is counterintuitive. The large contrast in atomic radii between Ca^{2+} and Zr^{4+} (1.00 and 0.72 Å, respectively)[45] should favor cation ordering as observed in CaTiN$_2$, SrZrN$_2$, and BaZrN$_2$.[41,43,57] Indeed, through the use of DFT and cluster expansion, we found that the ground state configuration is strongly favored at 1,300 K (Figure S21). If CaZrN$_2$ were in thermodynamic equilibrium, then there would be an insignificant degree of cation disorder.

To relate these predictions to experimental observations, we simulated PXRD patterns across all 24-atom configurations and ensemble averaged them for the temperatures of interest (Figure 7). As expected for increasing disorder, the reflection
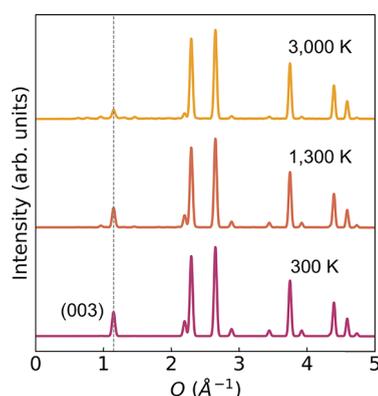
Figure 7. Simulated diffraction patterns for the thermodynamic ground state of CaZrN$_2$, calculated as a function of the temperature from the ensemble average. The supercell reflection at $Q = 1.1$ Å corresponding to the (003) plane of the fully ordered ($R\overline{3}m$) structure persists even up to 3,000 K.

from the (003) plane in the ordered structure (arising from cation layering) decays in intensity with increasing temperature. Temperatures generated from DFT can be offset a couple hundred degrees from experiment,[63] but the range from 300 to 3,000 K safely encompasses the synthesis temperature of 1,300 K. The (003) peak in the simulated patterns is significant even at 3,000 K, suggesting that the ordering in CaZrN$_2$ would be observed in the XRD pattern if the system were fully in thermodynamic equilibrium.

The SXRD pattern of experimentally synthesized CaZrN$_2$ does not show this low-angle peak (Figure 2), indicating that this cation-disordered CaZrN$_2$ is far from thermodynamic equilibrium. This hypothesis can be supported due to the short synthesis times relative to the slow rate of diffusion in nitrides.[64] Here we demonstrate an instance of a short metathesis reaction kinetically trapping disorder in a ternary nitride. Further annealing or higher synthesis temperatures could produce cation ordering in CaZrN$_2$, as seen in ZnGeN$_2$ and ZnGeP$_2$.[65,66]

This finding highlights that accounting for metastability is an area of further growth for predictive synthesis. As with thin film sputtering,[15] bulk syntheses involve myriad thermodynamic

and kinetic factors that influence final product formation. While computational techniques to account for temperature effects on enthalpy have been developed,[67] entropic contributions (e.g., compositional and configurational disorder) are not yet included in these chemical potential diagrams as they are computationally expensive to calculate. This gap motivates further work to align computational and synthetic techniques to bring about a truly predictive synthesis paradigm.

■ CONCLUSION

We report the discovery of two new ternary nitrides, CaZrN$_2$ and CaHfN$_2$, via mechanistically guided metathesis synthesis of bulk powders. These phases crystallize in the cation-disordered rocksalt structure ($Fm\overline{3}m$), as opposed to the computationally predicted α-NaFeO$_2$ structure type ($R\overline{3}m$). *In situ* synchrotron powder X-ray diffraction analysis shows how Zr^{3+} intermediates form early on in the reaction process, which rationalizes why an excess of the Ca$_3$N$_2$ reagent is synthetically necessary to generate a higher chemical potential of nitrogen. These findings stand in contrast to our prior synthesis of MgZrN$_2$, which proceeds stoichiometrically from 2 Mg$_2$NCl + ZrCl$_4$ to MgZrN$_2$ + 2 MgCl$_2$ via a ZrNCl intermediate, so as to avoid any N$_2$ (g) linked redox chemistry. The observed synthetic pathways match well with the predictions generated from chemical potential diagrams. Additional thermodynamic calculations show that the observed $Fm\overline{3}m$ structure is metastable with respect to the ordered $R\overline{3}m$ structure, suggesting that the $R\overline{3}m$ structure may be achievable under different synthetic conditions. In summary, these findings demonstrate a generalizable strategy for predicting and conducting metathesis reactions with the goal of synthesizing new ternary nitrides: combine *in situ* SXRD studies with thermodynamic calculations for mechanistically guided materials chemistry.

■ EXPERIMENTAL SECTION

Synthesis. *Caution:* N$_2$ *gas formation within sealed ampules can cause explosions at high temperatures, and appropriate precautions should be taken to prevent equipment damage and unsafe conditions.*

All reagents are moisture-sensitive and were therefore handled in an argon-filled glovebox unless otherwise noted (O$_2$ < 0.1 ppm, H$_2$O < 0.5 ppm). Ca$_3$N$_2$ (Chem Cruz or Alfa Aesar, >98% metals basis), Mg$_3$N$_2$ (Alfa Aesar, >98% metals basis), and MgCl$_2$ (Sigma-Aldrich, anhydrous, >98% metals basis) were used as received. ZrCl$_4$ (Acros, 98%) and HfCl$_4$ (Sigma-Aldrich, 99% metals basis, except for Zr, with <2.7%) were purified by heating approximately 4 g in a sealed quartz ampule (10 mm inner diameter, 12 mm outer diameter, ca. 30 cm long) in a 3-zone horizontal tube furnace to transport ZrCl$_4$ from the hot zone (400 °C) to the colder zone (300 °C), leaving behind less volatile, oxide-based impurities (e.g., ZrO$_2$). CaCl$_2$ (anhydrous, Alfa Aesar, 98%) was dried under flowing Ar for 24 h at 300 °C.

Ca$_2$NCl was synthesized following a method adapted from literature.[68] Stoichiometric amounts of Ca$_3$N$_2$ and CaCl$_2$ were combined in an agate mortar and pestle and ground into a homogeneous pink powder (about 2 g). The powder was then cold pressed ($P \approx 300$ MPa) into a dense pellet (diameter = 0.25 in) and placed in a niobium tube (10 cm long, 0.375 in. outer diameter, 0.015 in. wall thickness). Prior to use, the surface oxide of the niobium was removed by scrubbing with an abrasive scour pad in the glovebox. The ends of the tube were crimped down using the arbor press. This ampule was then brought out of the glovebox and quickly sealed under an argon atmosphere via arc-melting of the crimped ends of the niobium. The sealed metal ampule was then sealed in a quartz ampule under vacuum and heated at 5 °C/min in a muffle furnace to a set point of 740 °C. The reaction was held at temperature for 50 h, and

then allowed to cool to room temperature before opening the ampule in the glovebox.

Mg_2NCl was synthesized following a method adapted from literature,[69] as we described previously.[40] Near stoichiometric amounts of Mg_3N_2 (ca. 3 g) and $MgCl_2$ (ca. 3 g) were combined in an agate mortar and pestle and ground into a homogeneous tan powder. A slight excess of $MgCl_2$ (ca. 1 mol %) was used to ensure complete conversion of the Mg_3N_2. The powder was then cold pressed ($P \approx 80$ MPa) into a dense pellet (diameter = 0.5 in.) and placed in a quartz ampule (14 mm i.d., 16 mm o.d.). This ampule was then brought out of the glovebox and quickly sealed under vacuum (≤ 20 mTorr, as determined by a Pirani gauge) by using an oxygen/methane torch. The sealed ampule (ca. 15 cm^3 internal volume) was then heated at 10 °C/min in a muffle furnace to a set point of 550 °C. The reaction was held at that temperature for 5 days and then allowed to cool to room temperature before opening the ampule in the glovebox.

Reaction mixtures targeting $CaZrN_2$ and $CaHfN_2$ were prepared by combining the desired reagents in specific mole ratios (e.g., 1.17 Ca_3N_2 + $ZrCl_4$, as specified in the text) and homogenizing with an agate mortar and pestle. Reaction scales ranged from ca. 50 mg to ca. 500 mg total charge of reactants. Reaction mixtures were loaded into crucibles as loose powders or as 0.25 in. diameter pellets (cold pressed at 300 MPa) and sealed under vacuum in quartz ampules (<30 mTorr). Many syntheses were conducted using alumina crucibles, but optimized syntheses used homemade stainless steel crucibles to minimize oxygen contamination. These steel crucibles were made from stainless steel tubes (3/8 in outer diameter, 0.020 in wall thickness, TP-304L), welded closed on one end and left open on the other. The optimized synthesis involved pelletized reaction mixtures (ca. 500 mg) held in the steel crucibles nested inside quartz ampules along with a 1 g graphite rod as an oxygen getter, physically separated from the pellet. These ampules were transferred from the glovebox to a vacuum manifold using a custom air-free transfer valve, and flame-sealed under vacuum (<30 mTorr) using an oxygen/methane torch. Optimized reactions were heated in a muffle furnace at +5 °C/min to the specified dwell temperature, allowed to thermally equilibrate for 10 min, and then air-quenched by removing the ampule from the furnace and placing it in an insulating brick holder on the benchtop. Other synthesis conditions are specified in the text where relevant. The products are moisture sensitive. To remove byproduct $CaCl_2$ from the target compounds, samples were washed with anhydrous methanol (dried over molecular sieves for at least 5 days)[70] in an argon glovebox.

X-ray Diffraction Experiments. The products of all reactions were characterized by powder X-ray diffraction (PXRD). PXRD measurements were performed by using a Bruker DaVinci diffractometer with Cu Kα X-ray radiation. Prior to collecting PXRD, silicon powder was ground in with the reaction products as an internal standard for lattice parameters. All samples were prepared for PXRD from within the glovebox by placing powder on off-axis cut silicon single crystal wafers to reduce the background and then covered with polyimide tape to slow exposure to the atmosphere.

High-resolution synchrotron powder X-ray diffraction (SXRD) measurements on select samples were conducted via the mail-in program at the 11-BM-B end station of the Advanced Photon Source at Argonne National Laboratory.[71] Samples were prepared by loading reaction products (from optimized synthetic conditions) into extruded quartz capillaries (0.69 mm inner diameter, 0.7 mm outer diameter), which were subsequently nested inside kapton capillaries for measurement. Data were collected at $\lambda \approx 0.459$ Å. SXRD patterns are shown in Q-space to account for a small difference in wavelength between measurements ($Q = 4\pi \sin(\theta)/\lambda$).

In situ SXRD was conducted at the 17-BM-B end station of the Advanced Photon Source at Argonne National Laboratory ($\lambda = 0.24101$ Å). Samples were prepared by loading reaction mixtures into extruded quartz capillaries (0.9 mm inner diameter, 1.1 mm outer diameter) and flame-sealing under vacuum (<30 mTorr). Capillaries were loaded into a flow-cell apparatus[72] and heated at 5 °C/min to the specified temperature. *Caution: N_2 gas formation within the capillary can cause it to break at high temperatures.* Diffraction pattern images were collected using a PerkinElmer plate detector positioned 700 mm away from the sample. Images were collected every 30 s by summing 20 exposures of 0.5 s each, followed by 20 s of deadtime. Images collected from the plate detector were radially integrated by using GSAS-II and calibrated by using a silicon standard.

X-ray Diffraction Analysis. Quantitative phase analysis of PXRD and *in situ* SXRD data was conducted using the Rietveld method as implemented in TOPAS v6.[51] For laboratory-diffraction PXRD experiments (Bruker system, Cu Kα radiation), the sample displacement was first refined against the silicon standard. The sample displacement was then fixed, and the relevant phases were then refined. For each phase, lattice parameters, size broadening, and atomic thermal parameters were refined. A 10 term polynomial was used to fit the background.

High-resolution SXRD data sets were analyzed in a similar way to identify the cation occupancy for the $Ca_x M_{2-x} N_2$ phase in each sample (M = Zr, Hf). Cubic ZrN ($Fm\overline{3}m$) was used as a starting model, with Ca and Zr or Hf on the cation site with 50% occupancy each. Cation occupancy (x) was constrained to equal anion occupancy (i.e., Ca + M = N) during refinements. The anion site was fixed at full occupancy. The atomic displacement parameters were refined isotropically. Other relevant phases were also added to the model, and their lattice parameters, size broadening (Lorentzian) parameters, and atomic thermal parameters were refined. A broad background peak from the quartz capillary was modeled with a Lorentzian function, and the remaining background was modeled with a 10-term polynomial. The data sets were collected without an internal standard, and sample displacement was not refined during analysis.

Due to the number and positional overlap of intermediates during the sequential refinements, several variables were fixed to better compare phase fractions. Thermal displacement parameters were fixed at 1 Å^2 for each phase to better account for changes in the peak intensity during the reaction. Atoms were fixed at full occupancy for each site. RS phases were modeled as ZrN (i.e., metal site mixing was not refined). The crystalline size domain was fixed at 200 nm (as modeled using a Lorentzian polynomial) for most phases, except the ZrNCl and RS phases, which exhibited noticeable peak broadening. ZrNCl was refined using thermal displacement parameters that were fixed at 20 Å^2 and anisotropic size broadening. Size broadening for RS phases was manually refined from the final scan in the sequence and fixed for all other scans (crystallite size of ca. 7 nm). In order to compare the relative fractions of phases determined from Rietveld calculations, a weighted scale factor (W.S.F.) is defined as $Q_p = S_p \cdot V_p \cdot M_p$ where Q_p = weighted scale factor of phase p, S_p is scale factor calculated from Rietveld, V_p is the volume of the unit cell, and M_p is the atomic mass of the unit cell. It should be noted that we omit the Brindley coefficient for microabsorption correction in our calculation of W.S.F. due to the unreliable refinement of particle sizes for individual phases. Amorphous material and product lost as vapor are not accounted for in the sequential refinement; hence, we use the W.S.F. instead of relative wt % or mol %. We reference all phases by their nominal stoichiometric formula; however, the actual chemical formula may be distinct from the written formula, as XRD data alone cannot typically resolve nonstoichiometric compounds.

Thermodynamic Analysis. Thermodynamic calculations were performed using DFT-computed values and tools from the Materials Project (v2022.10.28) and pymatgen (v2023.9.10).[61,73] Reaction energies were calculated from the Gibbs formation energies as a function of temperature, using the method of Bartel et al.[67] Chemical potential diagrams were generated in the method of Yokokawa[23] as detailed by Todd et al.[24] and implemented in pymatgen. Mg_2NCl is calculated to be +0.02 eV/atom metastable relative to the binaries, which is within the DFT error of the convex hull. We therefore applied a small correction to bring the phase to the hull, allowing for visualization in the chemical potential diagrams. All other phases shown in Figures 6 and S21−S23 are calculated to be stable.

Thermodynamic Analysis of Disorder in $CaZrN_2$. To produce a training set for the cluster expansion, a number of DFT calculations

were conducted using VASP.[74] The PBE functional was used within the projector-augmented wave method.[75] A plane-wave cutoff of 400 eV was used. K-point densities were used such that the total energies were converged within 1 meV/atom. All structural degrees of freedom were allowed to be optimized within the structural relaxation (i.e., volume, cell shape, atom positions). Structures were generated using the pylada software.[76] To produce symmetry-inequivalent supercells, Hermite Normal Form transformation matrices were constructed using an algorithm developed by Hart and Forcade.[77] The transformation matrices were applied to the RS primitive cell to produce supercells with varying dimensions. The supercells were then decorated with different atomic orderings to make varying $CaZrN_2$ configurations.

The Alloy Theoretic Automated Toolkit (ATAT) was employed to fit a cluster expansion.[78,79] To ensure that the cluster expansion was properly representing the highly ordered configurations, we exhaustively enumerated all 8-atom and 12-atom $CaZrN_2$ configurations and included them in the training set. In total, the training set was made up of 70 symmetry inequivalent $CaZrN_2$ configurations, ranging in size from 8 to 24 atoms. A cross validation score of 10.4 meV/atom was obtained. Considering that the training set had an energy range of 324 meV/atom, we deemed the 10.4 meV/atom cross validation score to be sufficiently small. The energies of all 37,883 24-atom $CaZrN_2$ configurations were predicted using the fitted cluster expansion.

To ensemble average the XRD patterns, first the partition function, Z, was calculated using all 37,883 24-atom configurations

$$Z(T) = \sum_{i}^{37,883} e^{-E_i/k_B T} \tag{8}$$

Here, i is the index of the configuration, E_i is the total energy of the ith configuration, k_B is Boltzmann's constant, and T is the absolute temperature. The temperature-dependent probability of each configuration, $P_i(T)$, was then determined using the following equation

$$P_i(T) = \frac{e^{-E_i/k_B T}}{Z(T)} \tag{9}$$

Finally, the intensity of the ensemble-averaged XRD, I, was calculated as a function of temperature and wavenumber, Q:

$$I(Q, T) = \sum_{i}^{n} (I_i(Q) \cdot P_i(T)) \tag{10}$$

For a justification of ensemble averaging XRD patterns in the above way, see Jones et al.[80] The powder XRD pattern for each structure was generated with a Cu K_α wavelength using pymatgen.[73]

ASSOCIATED CONTENT

Supporting Information

The Supporting Information is available free of charge at https://pubs.acs.org/doi/10.1021/jacs.3c12114.

Optical property measurements, additional structural analysis of synchrotron PXRD data, compositional analysis, SEM/EDS analysis, XPS analysis, combustion analysis, influence of synthesis conditions on structure, control synthesis experiments, *in situ* synchrotron PXRD patterns, alternative hypotheses for reaction steps, thermodynamic analysis and *in situ* SXRD toward $ZnZrN_2$, thermodynamic analysis of cation (dis)order, additional thermodynamic analysis, reaction network analysis (PDF)

Accession Codes

CCDC 2304494−2304495 contain the supplementary crystallographic data for this paper. These data can be obtained free of charge via www.ccdc.cam.ac.uk/data_request/cif, or by

emailing data_request@ccdc.cam.ac.uk, or by contacting The Cambridge Crystallographic Data Centre, 12 Union Road, Cambridge CB2 1EZ, UK; fax: +44 1223 336033.

AUTHOR INFORMATION

Corresponding Author

James R. Neilson − *Department of Chemistry, Colorado State University, Fort Collins, Colorado 80523-1872, United States; School of Advanced Materials Discovery, Colorado State University, Fort Collins, Colorado 80523, United States;* ● orcid.org/0000-0001-9282-5752; Email: james.neilson@colostate.edu

Authors

Christopher L. Rom − *Department of Chemistry, Colorado State University, Fort Collins, Colorado 80523-1872, United States; Materials Science Center, National Renewable Energy Laboratory, Golden, Colorado 80401, United States;* ● orcid.org/0000-0002-6176-3197

Andrew Novick − *Department of Physics, Colorado School of Mines, Golden, Colorado 80401, United States*

Matthew J. McDermott − *Materials Sciences Division, Lawrence Berkeley National Laboratory, Berkeley, California 94720, United States; Department of Materials Science and Engineering, University of California, Berkeley, California 94720, United States;* ● orcid.org/0000-0002-4071-3000

Andrey A. Yakovenko − *X-ray Science Division, Advanced Photon Source, Argonne National Laboratory, Lemont, Illinois 60439, United States*

Jessica R. Gallawa − *Department of Chemistry, Colorado State University, Fort Collins, Colorado 80523-1872, United States*

Gia Thinh Tran − *Department of Chemistry, Colorado State University, Fort Collins, Colorado 80523-1872, United States;* ● orcid.org/0000-0002-3369-7321

Dominic C. Asebiah − *Department of Chemistry, Colorado State University, Fort Collins, Colorado 80523-1872, United States*

Emily N. Storck − *Department of Chemistry, Colorado State University, Fort Collins, Colorado 80523-1872, United States*

Brennan C. McBride − *Department of Chemistry, Colorado State University, Fort Collins, Colorado 80523-1872, United States;* ● orcid.org/0000-0002-3825-6138

Rebecca C. Miller − *Analytical Resources Core, Colorado State University, Fort Collins, Colorado 80523-1872, United States;* ● orcid.org/0000-0001-5263-7431

Amy L. Prieto − *Department of Chemistry, Colorado State University, Fort Collins, Colorado 80523-1872, United States;* ● orcid.org/0000-0001-9235-185X

Kristin A. Persson − *Molecular Foundry, Lawrence Berkeley National Laboratory, Berkeley, California 94720, United States; Department of Materials Science and Engineering, University of California, Berkeley, California 94720, United States;* ● orcid.org/0000-0003-2495-5509

Eric Toberer − *Department of Physics, Colorado School of Mines, Golden, Colorado 80401, United States*

Vladan Stevanović − *Department of Metallurgical and Materials Engineering, Colorado School of Mines, Golden, Colorado 80401, United States*

Andriy Zakutayev − *Materials Science Center, National Renewable Energy Laboratory, Golden, Colorado 80401, United States;* ● orcid.org/0000-0002-3054-5525

Complete contact information is available at:

pubs.acs.org/JACS

Article

Notes

The authors declare no competing financial interest.

■ ACKNOWLEDGMENTS

■ REFERENCES

(1) Kovnir, K. Predictive synthesis. *Chem. Mater.* **2021**, *33*, 4835−4841.

(2) Neilson, J. R.; McDermott, M. J.; Persson, K. A. Modernist materials synthesis: Finding thermodynamic shortcuts with hyper-dimensional chemistry. *J. Mater. Res.* **2023**, *38*, 2885−2893.

(3) Alberi, K.; Nardelli, M. B.; Zakutayev, A.; Mitas, L.; Curtarolo, S.; Jain, A.; Fornari, M.; Marzari, N.; Takeuchi, I.; Green, M. L.; et al. The 2019 materials by design roadmap. *J. Phys. D: Appl. Phys.* **2019**, *52*, 013001.

(4) Sun, W.; Bartel, C. J.; Arca, E.; Bauers, S. R.; Matthews, B.; Orvañanos, B.; Chen, B.-R.; Toney, M. F.; Schelhas, L. T.; Tumas, W.; et al. A map of the inorganic ternary metal nitrides. *Nat. Mater.* **2019**, *18*, 732−739.

(5) Walters, L. N.; Zhang, C.; Dravid, V. P.; Poeppelmeier, K. R.; Rondinelli, J. M. First-Principles Hydrothermal Synthesis Design to Optimize Conditions and Increase the Yield of Quaternary Heteroanionic Oxychalcogenides. *Chem. Mater.* **2021**, *33*, 2726−2741.

(6) Gautier, R.; Zhang, X.; Hu, L.; Yu, L.; Lin, Y.; Sunde, T. O.; Chon, D.; Poeppelmeier, K. R.; Zunger, A. Prediction and accelerated laboratory discovery of previously unknown 18-electron ABX compounds. *Nat. Chem.* **2015**, *7*, 308−316.

(7) Raccuglia, P.; Elbert, K. C.; Adler, P. D.; Falk, C.; Wenny, M. B.; Mollo, A.; Zeller, M.; Friedler, S. A.; Schrier, J.; Norquist, A. J. Machine-learning-assisted materials discovery using failed experiments. *Nature* **2016**, *533*, 73−76.

(8) Altman, A. B.; Tamerius, A. D.; Koocher, N. Z.; Meng, Y.; Pickard, C. J.; Walsh, J. P.; Rondinelli, J. M.; Jacobsen, S. D.; Freedman, D. E. Computationally directed discovery of MoBi$_2$. *J. Am. Chem. Soc.* **2021**, *143*, 214−222.

(9) Greenaway, A. L.; Ke, S.; Culman, T.; Talley, K. R.; Mangum, J. S.; Heinselman, K. N.; Kingsbury, R. S.; Smaha, R. W.; Gish, M. K.; Miller, E. M.; et al. Zinc Titanium Nitride Semiconductor toward Durable Photoelectrochemical Applications. *J. Am. Chem. Soc.* **2022**, *144*, 13673−13687.

(10) Heinselman, K. N.; Lany, S.; Perkins, J. D.; Talley, K. R.; Zakutayev, A. Thin Film Synthesis of Semiconductors in the Mg−Sb−N Materials System. *Chem. Mater.* **2019**, *31*, 8717−8724.

(11) Hinuma, Y.; Hatakeyama, T.; Kumagai, Y.; Burton, L. A.; Sato, H.; Muraba, Y.; Iimura, S.; Hiramatsu, H.; Tanaka, I.; Hosono, H.; et al. Discovery of earth-abundant nitride semiconductors by computational screening and high-pressure synthesis. *Nat. Commun.* **2016**, *7*, 1−10.

(12) Gvozdetskyi, V.; Bhaskar, G.; Batuk, M.; Zhao, X.; Wang, R.; Carnahan, S. L.; Hanrahan, M. P.; Ribeiro, R. A.; Canfield, P. C.; Rossini, A. J.; et al. Computationally driven discovery of a family of layered LiNiB polymorphs. *Angew. Chem., Int. Ed.* **2019**, *58*, 15855−15862.

(13) Gvozdetskyi, V.; Wang, R.; Xia, W.; Zhang, F.; Lin, Z.; Ho, K.-M.; Miller, G.; Zaikina, J. V. How to Look for Compounds: Predictive Screening and in situ Studies in Na-Zn-Bi System. *Chemistry—A European Journal* **2021**, *27*, 15954−15966.

(14) Zakutayev, A.; Zhang, X.; Nagaraja, A.; Yu, L.; Lany, S.; Mason, T. O.; Ginley, D. S.; Zunger, A. Theoretical prediction and experimental realization of new stable inorganic materials using the inverse design approach. *J. Am. Chem. Soc.* **2013**, *135*, 10048−10054.

(15) Woods-Robinson, R.; Stevanović, V.; Lany, S.; Heinselman, K. N.; Horton, M. K.; Persson, K. A.; Zakutayev, A. Role of disorder in the synthesis of metastable zinc zirconium nitrides. *Physical Review Materials* **2022**, *6*, 043804.

(16) Chen, B.-R.; Lany, S.; Kelly, L. L.; Arca, E.; Iguchi, Y.; Perkins, J. D.; Yanagi, H.; Toney, M. F.; Schelhas, L. T.; Zakutayev, A. Antimony nitride discovered by theoretical structure prediction, rapid thermal annealing, and in situ X-ray diffraction. *Cell Reports Physical Science* **2022**, *3*, 100980.

(17) McDermott, M. J.; McBride, B. C.; Regier, C. E.; Tran, G. T.; Chen, Y.; Corrao, A. A.; Gallant, M. C.; Kamm, G. E.; Bartel, C. J.; Chapman, K. W.; et al. Assessing Thermodynamic Selectivity of Solid-State Reactions for the Predictive Synthesis of Inorganic Materials. *ACS Central Science* **2023**, *9*, 1957−1975.

(18) Shoemaker, D. P.; Hu, Y.-J.; Chung, D. Y.; Halder, G. J.; Chupas, P. J.; Soderholm, L.; Mitchell, J.; Kanatzidis, M. G. In situ studies of a platform for metastable inorganic crystal growth and materials discovery. *Proc. Natl. Acad. Sci. U. S. A.* **2014**, *111*, 10922−10927.

(19) Haynes, A. S.; Stoumpos, C. C.; Chen, H.; Chica, D.; Kanatzidis, M. G. Panoramic synthesis as an effective materials discovery tool: the system Cs/Sn/P/Se as a test case. *J. Am. Chem. Soc.* **2017**, *139*, 10814−10821.

(20) McClain, R.; Malliakas, C. D.; Shen, J.; He, J.; Wolverton, C.; González, G. B.; Kanatzidis, M. G. Mechanistic insight of KBiQ$_2$ ($Q =$ S, Se) using panoramic synthesis towards synthesis-by-design. *Chemical Science* **2021**, *12*, 1378−1391.

(21) Ito, H.; Shitara, K.; Wang, Y.; Fujii, K.; Yashima, M.; Goto, Y.; Moriyoshi, C.; Rosero-Navarro, N. C.; Miura, A.; Tadanaga, K. Kinetically Stabilized Cation Arrangement in Li$_3$YCl$_6$ Superionic Conductor during Solid-State Reaction. *Advanced Science* **2021**, *8*, 2101413.

(22) Quintero, M. A.; Shen, J.; Laing, C. C.; Wolverton, C.; Kanatzidis, M. G. Cubic Stuffed-Diamond Semiconductors Li-

Cu_3TiQ_4 (Q = S, Se, and Te). *J. Am. Chem. Soc.* **2022**, *144*, 12789−12799.

(23) Yokokawa, H. Generalized chemical potential diagram and its applications to chemical reactions at interfaces between dissimilar materials. *J. Phase Equilib.* **1999**, *20*, 258−287.

(24) Todd, P. K.; McDermott, M. J.; Rom, C. L.; Corrao, A. A.; Denney, J. J.; Dwaraknath, S. S.; Khalifah, P. G.; Persson, K. A.; Neilson, J. R. Selectivity in Yttrium manganese oxide synthesis via local chemical potentials in hyperdimensional phase space. *J. Am. Chem. Soc.* **2021**, *143*, 15185−15194.

(25) Rumble, J. R., Ed. *Bond Dissociation Energies in Diatomic Molecules" in CRC Handbook of Chemistry and Physics*, 104th ed. (Internet Version). https://hbcp.chemnetbase.com/documents/09_04/09_04_0001.xhtml?dswid=6263 (accessed October 23, 2023).

(26) Greenaway, A. L.; Melamed, C. L.; Tellekamp, M. B.; Woods-Robinson, R.; Toberer, E. S.; Neilson, J. R.; Tamboli, A. C. Ternary nitride materials: Fundamentals and emerging device applications. *Annu. Rev. Mater. Res.* **2021**, *51*, 591−618.

(27) Niewa, R.; Jacobs, H. Group V and VI alkali nitridometalates: a growing class of compounds with structures related to silicate chemistry. *Chem. Rev.* **1996**, *96*, 2053−2062.

(28) Sun, W.; Holder, A.; Orvañanos, B.; Arca, E.; Zakutayev, A.; Lany, S.; Ceder, G. Thermodynamic routes to novel metastable nitrogen-rich nitrides. *Chem. Mater.* **2017**, *29*, 6936−6946.

(29) Zakutayev, A.; Bauers, S. R.; Lany, S. Experimental Synthesis of Theoretically Predicted Multivalent Ternary Nitride Materials. *Chem. Mater.* **2022**, *34*, 1418−1438.

(30) Elder, S.; DiSalvo, F.; Topor, L.; Navrotsky, A. Thermodynamics of ternary nitride formation by ammonolysis: application to lithium molybdenum nitride ($LiMoN_2$), sodium tungsten nitride (Na_3WN_3), and sodium tungsten oxide nitride (Na_3WO_3N). *Chem. Mater.* **1993**, *5*, 1545−1553.

(31) Rognerud, E. G.; Rom, C. L.; Todd, P. K.; Singstock, N. R.; Bartel, C. J.; Holder, A. M.; Neilson, J. R. Kinetically controlled low-temperature solid-state metathesis of manganese nitride Mn_3N_2. *Chem. Mater.* **2019**, *31*, 7248−7254.

(32) Nakamura, S. Nobel Lecture: Background story of the invention of efficient blue InGaN light emitting diodes. *Rev. Mod. Phys.* **2015**, *87*, 1139.

(33) Gharavi, M. A.; Armiento, R.; Alling, B.; Eklund, P. Theoretical study of phase stability, crystal and electronic structure of MeMgN$_2$ (Me = Ti, Zr, Hf) compounds. *J. Mater. Sci.* **2018**, *53*, 4294−4305.

(34) Sarmiento-Perez, R.; Cerqueira, T. F.; Körbel, S.; Botti, S.; Marques, M. A. Prediction of stable nitride perovskites. *Chem. Mater.* **2015**, *27*, 5957−5963.

(35) Ching, W.; Mo, S.-D.; Tanaka, I.; Yoshiya, M. Prediction of spinel structure and properties of single and double nitrides. *Phys. Rev. B* **2001**, *63*, 064102.

(36) Greenaway, A. L.; Loutris, A. L.; Heinselman, K. N.; Melamed, C. L.; Schnepf, R. R.; Tellekamp, M. B.; Woods-Robinson, R.; Sherbondy, R.; Bardgett, D.; Bauers, S.; Zakutayev, A.; Christensen, S. T.; Lany, S.; Tamboli, A. C.; et al. Combinatorial synthesis of magnesium tin nitride semiconductors. *J. Am. Chem. Soc.* **2020**, *142*, 8421−8430.

(37) Kawamura, F.; Imura, M.; Murata, H.; Yamada, N.; Taniguchi, T. Synthesis of a Novel Rocksalt-Type Ternary Nitride Semiconductor $MgSnN_2$ Using the Metathesis Reaction Under High Pressure. *Eur. J. Inorg. Chem.* **2020**, *2020*, 446−451.

(38) Kawamura, F.; Murata, H.; Imura, M.; Yamada, N.; Taniguchi, T. Synthesis of $CaSnN_2$ via a high-pressure metathesis reaction and the properties of II-Sn-N$_2$ (II= Ca, Mg, Zn) semiconductors. *Inorg. Chem.* **2021**, *60*, 1773−1779.

(39) Bauers, S. R.; Holder, A.; Sun, W.; Melamed, C. L.; Woods-Robinson, R.; Mangum, J.; Perkins, J.; Tumas, W.; Gorman, B.; Tamboli, A.; Ceder, G.; Lany, S.; Zakutayev, A.; et al. Ternary nitride semiconductors in the rocksalt crystal structure. *Proc. Natl. Acad. Sci. U. S. A.* **2019**, *116*, 14829−14834.

(40) Rom, C. L.; Fallon, M. J.; Wustrow, A.; Prieto, A. L.; Neilson, J. R. Bulk Synthesis, Structure, and Electronic Properties of Magnesium

Zirconium Nitride Solid Solutions. *Chem. Mater.* **2021**, *33*, 5345−5354.

(41) Li, X.; Wang, X.; Han, Y.; Jing, X.; Huang, Q.; Kuang, X.; Gao, Q.; Chen, J.; Xing, X. High-dielectric-permittivity layered nitride $CaTiN_2$. *Chem. Mater.* **2017**, *29*, 1989−1993.

(42) Gregory, D.; Barker, M.; Edwards, P.; Siddons, D. Synthesis and structure of the new ternary nitride $SrTiN_2$. *Inorg. Chem.* **1998**, *37*, 3775−3778.

(43) Gregory, D.; Barker, M.; Edwards, P.; Siddons, D. Synthesis and structure of two new layered ternary nitrides, $SrZrN_2$ and $SrHfN_2$. *Inorg. Chem.* **1996**, *35*, 7608−7613.

(44) Shiraishi, A.; Kimura, S.; He, X.; Watanabe, N.; Katase, T.; Ide, K.; Minohara, M.; Matsuzaki, K.; Hiramatsu, H.; Kumigashira, H.; Hosono, H.; Kamiya, T.; et al. Design, Synthesis, and Optoelectronic Properties of the High-Purity Phase in Layered AETMN_2 (AE = Sr, Ba; TM = Ti, Zr, Hf) Semiconductors. *Inorg. Chem.* **2022**, *61*, 6650−6659.

(45) Shannon, R. T.; Prewitt, C. T. Effective ionic radii in oxides and fluorides. *Acta Crystallographica Section B: Structural Crystallography and Crystal Chemistry* **1969**, *25*, 925−946.

(46) Orisakwe, E.; Fontaine, B.; Gregory, D. H.; Gautier, R.; Halet, J.-F. Theoretical study on the structural, electronic and physical properties of layered alkaline-earth-group-4 transition-metal nitrides AEMN$_2$. *RSC Adv.* **2014**, *4*, 31981−31987.

(47) Hunting, J. L.; Szymanski, M. M.; Johnson, P. E.; Brenhin Kellar, C.; DiSalvo, F. J. The synthesis and structural characterization of the new ternary nitrides: Ca_4TiN_4 and Ca_5NbN_5. *J. Solid State Chem.* **2007**, *180*, 31−40.

(48) Masood, H.; Yunus, R.; Choong, T. S.Y.; Rashid, U.; Taufiq Yap, Y. H. Synthesis and characterization of calcium methoxide as heterogeneous catalyst for trimethylolpropane esters conversion reaction. *Applied Catalysis A: General* **2012**, *425*, 184−190.

(49) Schneider, J. D.; Agocs, D. B.; Prieto, A. L. Design of a Sample Transfer Holder to Enable Air-Free X-ray Photoelectron Spectroscopy. *Chem. Mater.* **2020**, *32*, 8091−8096.

(50) Fairley, N.; Fernandez, V.; Richard-Plouet, M.; Guillot-Deudon, C.; Walton, J.; Smith, E.; Flahaut, D.; Greiner, M.; Biesinger, M.; Tougaard, S.; Morgan, D.; Baltrusaitis, J.; et al. Systematic and collaborative approach to problem solving using X-ray photoelectron spectroscopy. *Applied Surface Science Advances* **2021**, *5*, 100112.

(51) Coelho, A. A. TOPAS and TOPAS-Academic: an optimization program integrating computer algebra and crystallographic objects written in C++. *J. Appl. Crystallogr.* **2018**, *51*, 210−218.

(52) Azdad, Z.; Marot, L.; Moser, L.; Steiner, R.; Meyer, E. Valence band behaviour of zirconium oxide, Photoelectron and Auger spectroscopy study. *Sci. Rep.* **2018**, *8*, 16251.

(53) Christensen, A. A. A Neutron Diffraction Investigation on Single Crystals of Titanium Carbide, Titanium Nitride, and Zirconium Nitride. *Acta Chem. Scand.* **1975**, *29a*, 563−564.

(54) Aigner, K.; Lengauer, W.; Rafaja, D.; Ettmayer, P. Lattice parameters and thermal expansion of $Ti(C_xN_{1-x})$, $Zr(C_xN_{1-x})$, $Hf(C_xN_{1-x})$ and TiN_{1-x} from 298 to 1473 K as investigated by high-temperature X-ray diffraction. *J. Alloys Compd.* **1994**, *215*, 121−126.

(55) Martinolich, A. J.; Kurzman, J. A.; Neilson, J. R. Circumventing diffusion in kinetically controlled solid-state metathesis reactions. *J. Am. Chem. Soc.* **2016**, *138*, 11031−11037.

(56) Gillan, E. G.; Kaner, R. B. Synthesis of refractory ceramics via rapid metathesis reactions between solid-state precursors. *Chem. Mater.* **1996**, *8*, 333−343.

(57) Gregory, D. H.; Barker, M. G.; Siddons, D. J.; Edwards, P. P.; Slaski, M. Synthesis, Structure and Magnetic Properties of the Group IV Ternary Nitrides, AMN_2 (A = Alkaline Earth Metal, M = Transition Metal). *MRS Online Proceedings Library (OPL)* **1998**, *547*, 401−406.

(58) Todd, P. K.; Fallon, M. J.; Neilson, J. R.; Zakutayev, A. Two-step solid-state synthesis of ternary nitride materials. *ACS Materials Letters* **2021**, *3*, 1677−1683.

(59) Salyulev, A.; Vovkotrub, E.; Strekalovsky, V. *Raman Spectra of Complex Compounds MeMCl₆ (Me²⁺-Alkali-Earth or Transition Metal, M-Sn, Ti, Zr, Hf)*; International Conference on Raman Spectroscopy: 1998; pp 714−715.

(60) Houska, C. Thermal expansion and atomic vibration amplitudes for TiC, TiN, ZrC, ZrN, and pure tungsten. *J. Phys. Chem. Solids* **1964**, *25*, 359−366.

(61) Jain, A.; Ong, S. P.; Hautier, G.; Chen, W.; Richards, W. D.; Dacek, S.; Cholia, S.; Gunter, D.; Skinner, D.; Ceder, G.; Persson, K. A.; et al. Commentary: The Materials Project: A materials genome approach to accelerating materials innovation. *APL Materials* **2013**, *1*, 011002.

(62) McDermott, M. J.; Dwaraknath, S. S.; Persson, K. A. A graph-based network for predicting chemical reaction pathways in solid-state materials synthesis. *Nat. Commun.* **2021**, *12*, 1−12.

(63) Novick, A.; Nguyen, Q.; Garnett, R.; Toberer, E.; Stevanović, V. Simulating high-entropy alloys at finite temperatures: An uncertainty-based approach. *Physical Review Materials* **2023**, *7*, 063801.

(64) Schnepf, R. R.; Cordell, J. J.; Tellekamp, M. B.; Melamed, C. L.; Greenaway, A. L.; Mis, A.; Brennecka, G. L.; Christensen, S.; Tucker, G. J.; Toberer, E. S.; Lany, S.; Tamboli, A. C.; et al. Utilizing site disorder in the development of new energy-relevant semiconductors. *ACS Energy Letters* **2020**, *5*, 2027−2041.

(65) Blanton, E. W.; He, K.; Shan, J.; Kash, K. Characterization and control of ZnGeN₂ cation lattice ordering. *J. Cryst. Growth* **2017**, *461*, 38−45.

(66) Schnepf, R. R.; Martinez, A. D.; Mangum, J. S.; Schelhas, L. T.; Toberer, E. S.; Tamboli, A. C. Disorder-tunable ZnGeP₂ for epitaxial top cells on Si. *2019 IEEE 46th Photovoltaic Specialists Conference (PVSC)*; 2019; pp 1052−1055.

(67) Bartel, C. J.; Millican, S. L.; Deml, A. M.; Rumptz, J. R.; Tumas, W.; Weimer, A. W.; Lany, S.; Stevanović, V.; Musgrave, C. B.; Holder, A. M. Physical descriptor for the Gibbs energy of inorganic crystalline solids and temperature-dependent materials chemistry. *Nat. Commun.* **2018**, *9*, 4168.

(68) Hadenfeldt, C.; Herdejürgen, H. Darstellung und Kristallstruktur der Calciumnitridhalogenide Ca₂NCl und Ca₂NBr. *Zeitschrift für anorganische und allgemeine Chemie* **1987**, *545*, 177−183.

(69) Li, Y.; George, J.; Liu, X.; Dronskowski, R. Synthesis, structure determination and electronic structure of magnesium nitride chloride, Mg₂NCl. *Zeitschrift für anorganische und allgemeine Chemie* **2015**, *641*, 266−269.

(70) Williams, D. B. G.; Lawton, M. Drying of organic solvents: quantitative evaluation of the efficiency of several desiccants. *Journal of Organic Chemistry* **2010**, *75*, 8351−8354.

(71) Wang, J.; Toby, B. H.; Lee, P. L.; Ribaud, L.; Antao, S. M.; Kurtz, C.; Ramanathan, M.; Von Dreele, R. B.; Beno, M. A. A dedicated powder diffraction beamline at the Advanced Photon Source: Commissioning and early operational results. *Rev. Sci. Instrum.* **2008**, *79*, 085105.

(72) Chupas, P. J.; Chapman, K. W.; Kurtz, C.; Hanson, J. C.; Lee, P. L.; Grey, C. P. A versatile sample-environment cell for non-ambient X-ray scattering experiments. *J. Appl. Crystallogr.* **2008**, *41*, 822−824.

(73) Ong, S. P.; Richards, W. D.; Jain, A.; Hautier, G.; Kocher, M.; Cholia, S.; Gunter, D.; Chevrier, V. L.; Persson, K. A.; Ceder, G. Python Materials Genomics (pymatgen): A robust, open-source python library for materials analysis. *Comput. Mater. Sci.* **2013**, *68*, 314−319.

(74) Kresse, G.; Furthmüller, J. Efficiency of ab-initio total energy calculations for metals and semiconductors using a plane-wave basis set. *Comput. Mater. Sci.* **1996**, *6*, 15−50.

(75) Blöchl, P. E. Projector augmented-wave method. *Phys. Rev. B* **1994**, *50*, 17953−17979.

(76) d'Avezac, M.; Graf, P.; Paudal, T.; Peng, H.; Zhang, L.; Stephen, S.; Stevanovic, V. Pylada: a Comprehensive Python Framework for Preparing, Running, Monitoring, Analyzing, and Archiving High Throughput First Principles Calculations. https://github.com/pylada/pyladada-light (Accessed January 30, 2023).

(77) Hart, G. L. W.; Forcade, R. W. Algorithm for generating derivative structures. *Phys. Rev. B* **2008**, *77*, 224115.

(78) Van De Walle, A.; Asta, M.; Ceder, G. The alloy theoretic automated toolkit: A user guide. *Calphad* **2002**, *26*, 539−553.

(79) van de Walle, A.; Ceder, G. Automating first-principles phase diagram calculations. *J. Phase Equilib.* **2002**, *23*, 348.

(80) Jones, E. B.; Stevanović, V. The glassy solid as a statistical ensemble of crystalline microstates. *npj Computational Materials* **2020**, *6*, 56.